Journal of Materials Science: Materials in Electronics (2020) 31:8727–8736
https://doi.org/10.1007/s10854-020-03407-6

Enhanced electrical conductivity and multiferroic property of cobalt-doped bismuth ferrite nanoparticles

M. M. Rhaman[1,2] · M. A. Matin[1] · M. A. Al Mamun[1] · A. Hussain[1] · M. N. Hossain[1] · B. C. Das[3] · M. A. Hakim[1] · M. F. Islam[1]

Received: 14 June 2019 / Accepted: 13 April 2020 / Published online: 20 April 2020

Abstract
Multiferroic pure and cobalt-doped bismuth ferrite nanoparticles were synthesized by sol–gel method. The X-ray diffraction study showed a distinct crystalline phase with rhombohedral R3c structure. Rietveld refinement confirmed the reduction of crystallite size from 68 to 45 nm in doped BFO. Transmission electron microscopy was performed to confirm the morphology and lattice constant of the pure and cobalt-doped bismuth ferrite nanoparticles. The results of lattice constant have also been compared with the XRD results. Dielectric properties such as resistance, reactance, impedance, and resistivity were significantly decreased in doped BFO to 7.5 MΩ, 14 MΩ, 17 MΩ, 3.7 MΩ-m, respectively, at 100 Hz with concurrent increased conductivity of 0.184 (S/m) $\times 10^{-3}$ at 10 MHz. The ferroelectric properties of pure and doped samples exhibited significantly enhanced maximum polarization and coercive field in doped BFO of 16 μC/cm^2 and 6.2 kV/cm, respectively, at an applied field of 15 kV/cm. Ferromagnetic measurements of synthesized cobalt-doped BFO nanoparticles displayed a substantial improvement in saturation magnetization and coercive force of 7.07 emu/gm and 0.9 kOe, respectively. The important enhancement of magnetic properties with moderate value of coercive field of the cobalt-doped samples may have potential applications in spintronics and memory devices.

1 Introduction

Bismuth ferrite is a rare multiferroic material that simultaneously displays the ferroelectric and ferromagnetic properties in a single phase at room temperature that has drawn significant interest due to its prospective applications in spintronic devices, sensors, photovoltaic solar cells and microwave absorber [1–7]. The concurrent requirement of unfilled and partially filled d-orbital for multiferroic ordering makes BFO rare in nature [8]. In the view of practical applications, BFO stands out tall from all other perovskites (ABO_3) type multiferroic materials due to its high ferroelectric Curie temperature (T_C) of 1103 K and ferromagnetic Neel temperature (T_N) of 643 K [9]. Relatively low conductivity in BFO becomes a barrier for photovoltaic cells application. Thus, it can be expected that the conductivity of BFO is controlled by doping concentration. Many elements such as Ba [10], Co [11], Cr [12], La [13], Ni [14], Mn [15] have been doped in BFO to understand their responses to dielectric, electric, and multiferroic properties.

The enhancement of ferroelectric property in pure BFO has been realized that makes it suitable for possible application in device [9]. However, the maximum polarization and saturation magnetization of BFO are very low compared to many other standard multiferroic materials [16]. This is because of the canting effect of the Fe^{3+} sublattice moment and superimposition of a spiral spin structure (SSS) on antiferromagnetic order of BFO [16–18]. For practical use of BFO in devices, it is essential to know how to improve the magnetic properties without hampering the ferroelectric properties. The modification of SSS can also be attained by doping with transition metal into the B-Site (Fe^{3+}-site) of BFO liberating locked magnetization, consequently revealing poor ferromagnetism [19–21]. Cobalt (Co) is a unique transition metal which is magnetically active and doping in multiferroic materials may produce some modifications in the physical properties such as electronic transitions,

✉ M. M. Rhaman
mizan.eee@aust.edu

[1] Department of Glass and Ceramic Engineering, Bangladesh University of Engineering and Technology, Dhaka, Bangladesh

[2] Department of Electrical and Electronic Engineering, Ahsanullah University of Science and Technology, Dhaka, Bangladesh

[3] Department of Physics, Bangladesh University of Engineering and Technology, Dhaka, Bangladesh

ferromagnetic, and ferroelectric properties. Therefore, the induced electric potential can change the magnetization and the external magnetic force can excite electric polarization. The intrinsic coupling among ferroelectric and ferromagnetic properties of these novel materials is appropriate for spintronics and memory devices [22]. In pure BFO, Fe^{3+} spin is enclosed by 6 antiparallel spins at the adjacent Fe neighbors, resulting in a G-type antiferromagnetism. That means the Fe magnetic moments are joined ferromagnetically into the pseudocubic planes (111) and antiferromagnetically among nearest planes.

Fe and Co are the most common transition metals. Fe exhibits three crystal structures, namely (i) α-Fe, (ii) γ-Fe, and (iii) δ-Fe. All forms of Fe attain ferromagnetism, malleability, good plasticity, and thermal conductivity. Similarly, Co metal also exhibits three crystal structures: (i) α-Co (Cubic system, $F\bar{m}3m$), Co (Hexagonal system, $P6_3mc$), and ε-Co (Hexagonal system, $P6_3/mmc$). Hexagonal form is the most common close-packed lattice. Co is hard with permanent magnetism and high temperature resistance with good stability [23].

However, antiferromagnetic spiral spin modulated structure of pure BFO is tailored by a range of ($\lambda = 620 \pm 20$ Å) modulation guiding to SSS by the spiral direction of −[110] and the spin rotation plane (110) is leading to the cancelation of every macroscopic magnetization [24]. The domain walls of the pure BFO might show a weak ferromagnetization (Dzyaloshinski-Moriya theory) if the ferromagnetic moments are perpendicular in direction to [111] [25, 26]. Currently, it has been investigated that the improvement of multiferroic properties in pure BFO with decreasing the particle size [27]. The ionic radius of dopant Co^{2+} is 0.745 Å and base material Fe^{3+} is 0.645 Å; as a result, the particle size will be reduced with the increasing doping concentration. The Co^{3+} ions bond with O by sturdy covalence, whereas Co^{2+} is largely hybridized with the valence states of O. The Co have four band structure regions, i.e., Co^{2+} 3d *e* states, Co^{2+} 3d *e* and t_2 states, Co^{3+} 3d t_{2g} states, and combination of O 2p and Co^{2+}/Co^{3+} electronic states. The Co^{2+} 3d *e* states inhabit spin-down channel of Co^{2+} states, leading to local magnetic moment. However, Co^{3+} 3d *e* states are mainly above ε_F, while Co^{3+} 3d t_{2g} states are near to ε_F which causes to induce diamagnetism [23]. In addition, the ionic radius of Co^{2+} (0.745 Å) is much higher than Co^{3+} (0.545 Å) which influences more lattice distortion and increases bond angle of Fe–O–Fe with decreasing bond length of Fe–O. Thus, bandgap will be decreased and electrical conductivity will be increased [28]. Moreover, the electronic configurations of Co^{2+} and Co^{3+} are Co^{2+} [Ar] $3d^7$ and Co^{3+} [Ar] $3d^6$; due to crystal field splitting to minimize energy, Co^{2+} shows higher magnetic moment.

In this study, Co^{2+} as divalent transitional metal ions were selected to replace trivalent Fe^{3+} cations in pure BFO. In this study, pure $BiFeO_3$ (BFO), 5% Co^{2+} -doped $BiFe_{0.95}Co_{0.05}O_3$ (BFCO-5), 10% Co^{2+} -doped $BiFe_{0.9}Co_{0.1}O_3$ (BFCO-10), and 15% Co^{2+} -doped $BiFe_{0.85}Co_{0.15}O_3$ (BFCO-15) samples were synthesized by sol–gel method. The novelty of this research is the influence of Co^{2+} doping on electrical conductivity and multiferroic properties of BFO nanoparticles.

2 Sample preparation and methods

2.1 Sample preparation

Sol–gel method was used to synthesize pure and Co-doped BFO samples and annealed at 600 °C. Precursor materials used include bismuth nitrate pentahydrate ($Bi(NO_3)_3{\cdot}5H_2O$) (99% purity, Merck India), iron nitrate nonahydrate ($Fe(NO_3)_3{\cdot}9H_2O$) (98% purity, Merck India), and cobalt nitrate hexahydrate ($Co(NO_3)_2{\cdot}6H_2O$) (97% purity, Merck India). The details of sol–gel method can be found elsewhere [6]. The annealed nanoparticles were directly used for the analysis of magnetism. However, to conduct ferroelectric and leakage current analysis, it was essential to prepare cylindrical disk samples (pellet). 1 gm of nanoparticles was used to prepare a pellet. The pellet was pressed by a hydraulic press machine with 20 kN force for 1 min. The area and thickness of pellets were about 1.66 cm^2 and 0.13 cm. It was sintered again at 600 °C and conductive silver paste was then applied uniformly on both sides of the pellets. Furthermore, to measure dielectric properties, two very thin copper wires were joined on both sides of the tablets. Then, pellets were kept in an electric oven at 120 °C for 12 h.

2.2 Methods

The samples of $BiFe_{1-y}Co_yO_3$, where $y = 0, 0.05, 0.10, 0.15$ as BFO, BFCO-5, BFCO-10, and BFCO-15, were characterized to verify their structural and physical properties. The structural formation of pure and Co-doped BFO nanoparticles was analyzed by X-ray diffractometry (Model: PANalytical EMPYREAN, Netherlands). The morphology of nanoparticles were investigated by transmission electron microscopy (Model: Talos F200X). Dielectric properties of the samples were measured by an impedance analyzer (6500B Series, Wayne Kerr Electronics Ltd. UK). Ferroelectric properties and leakage current density were determined at room temperature by precision multiferroic loop tracer (Model: P-PMF, Radiant Tech. Inc., USA). Magnetic properties of the samples were measured at room temperature by vibrating sample magnetometer, VSM (Model no.: Micro Sense EV9, USA).

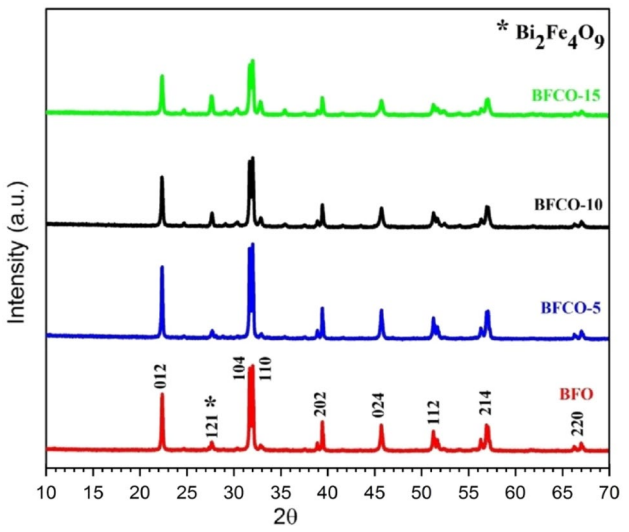

Fig. 1 XRD patterns with planes of BFO, BFCO-5, BFCO-10, and BFCO-15 nanoparticles

3 Results and discussion

3.1 X-ray diffraction

Figure 1 shows XRD patterns of pure and doped BFO nanoparticles. The patterns of pure BFO match well with crystalline rhombohedral structure with R3c space group and transformed to orthorhombic symmetry with $Pn2_1a$ space group for Co-doped BFO samples. The Rietveld refinement of the samples was conducted by HighScore Plus software. It is found that the crystallite size decreased from 68 to 45 nm and lattice strain increased from 0.186 to 0.28% with increasing Co concentration. Notably, the secondary phase (121) $Bi_2Fe_4O_9$ (*) became rich with increasing dopant concentration. $Bi_2Fe_4O_9$ was prominent at 27.7°. The combination of major phases and other secondary phases were also reported by researchers [29, 30].

3.2 Transmission electron microscopy

The transmission electron microscopy (TEM) images of pure and 15% Co-doped BFO nanoparticles are shown in Fig. 2a, b.

It was found that aggregated nanoparticles of both samples have irregular shape morphology, while the particle size of doped sample was found to be smaller than that of pure sample, and a similar trend was noticed in the SEM results [6]. The selected area electron diffraction (SAED) patterns of pure and doped samples are presented in Fig. 2c. Both samples appear to be polycrystalline in nature and the bright diffraction spots can be attributed to the crystallographic planes of (012), (104), (202), (024), (112), (214), and (220)

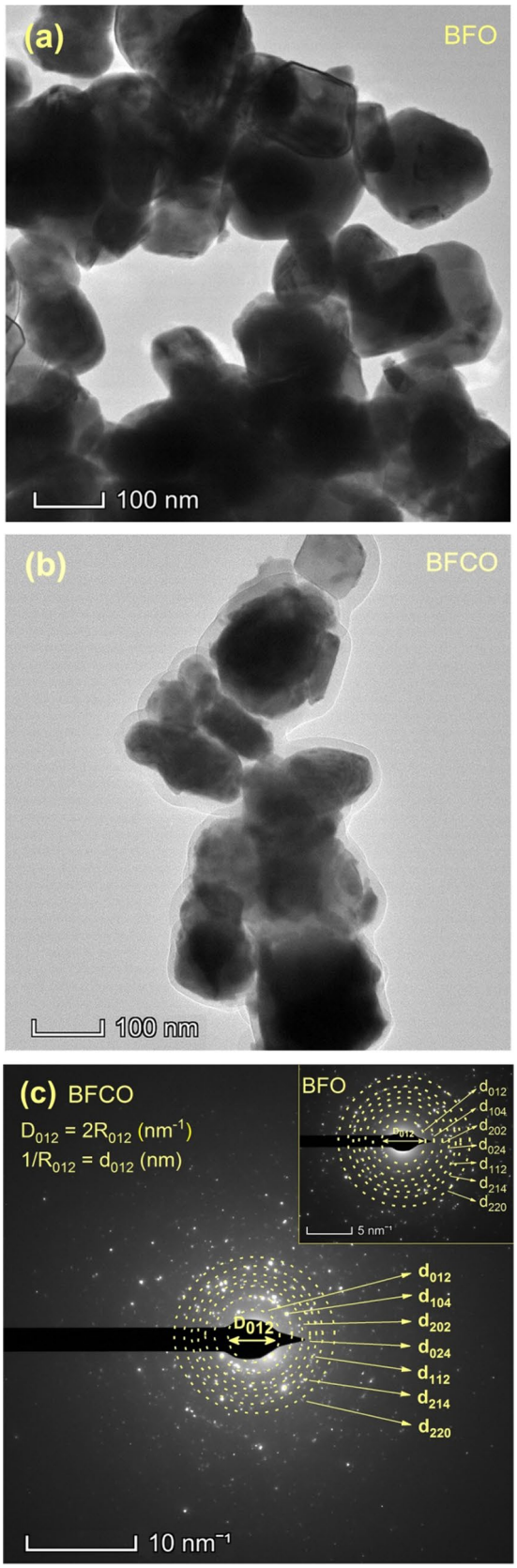

Fig. 2 TEM images of **a** pure BFO and **b** 15% Co-doped BFO nanoparticles, and **c** SAED pattern of 15% Co-doped BFO nanoparticles, inset shows the SAED pattern of pure BFO

which suggest that the doped sample mainly consists of BFO phase. The lattice constants were obtained using the interplanar spacing (d) values from SAED analysis using the following equation:

$$\frac{1}{d^2} = \frac{4}{3}\left(\frac{h^2 + hk + k^2}{a^2}\right) + \frac{l^2}{c^2} \quad (1)$$

Table 1 shows that the values of lattice constants are more or less similar to the values obtained from the XRD line profile analysis. However, the slight deviation in the values between XRD and SAED might be associated with the reason that the analyses were carried out for aggregated nanoparticles without any specific crystallographic orientation.

3.3 Electrical conductivity analysis

Dielectric properties such as resistance, reactance, impedance, AC resistivity, and AC conductivity are strongly correlated with electrical conductivity. The dielectric properties of materials are dominated by their electronic and crystal structures. It is a significant parameter for materials to design functional devices, particularly the electromagnetic devices. It controls the property of materials and devices such as energy conversion, extent of heat generation, and optical property [31]. The frequency-dependent dielectric properties were measured for pure and doped BFO nanoparticles. The range of measuring frequency was 20 Hz to 10 MHz. Figure 3a shows the variation of resistance (R) with frequency for pure and doped BFO samples; inset shows a close-up view. The amplitude of R was found to be considerably decreased with increasing Co concentration at frequency up to ~1 kHz. The plateau behavior of R was found at higher frequencies ($> 10^3$ Hz) which indicates possible discharge of space charge polarization or accumulation at boundaries region of homogeneous phases in the samples under external applied field [32, 33]. The values of R decreased with increasing Co dopant indicating the reduction of resistive properties and improvement of conductive properties for doped samples. The variation of reactance (X) with frequency exhibits the similar trend as resistance. Figure 3b shows the plot of reactance vs frequency for pure and doped BFO nanoparticles and its close view in inset. Evidently, the values of X were found to significantly decrease at low frequency and almost constant at high frequencies ($> 10^3$ Hz). The fundamental mechanism may be accounted for decreased X with increased conductivity across grain boundaries and enhanced charge carriers hopping among the localized ions at higher frequencies [34]. Moreover, the magnitude of X decreased with increasing Co doping level. With increasing Co concentration, the grain size of BFO decreases and thus X decreases [6]. This indicates the decrease in resistive path because of hindrance posed by the grain boundaries; a similar trend was found elsewhere [34]. The variation of reactance with resistance for pure and doped BFO samples is presented in Fig. 3c. It was observed that the reactance is directly proportional to resistance and the value of resistance is diminishing. The decreased values of reactance indicate the increased loss in resistance of the samples.

This behavior usually owes to the interplay of space charge polarization in the samples [35, 36].

Impedance analysis is an important metric to investigate the electrical conductivity of a material. It can ascertain the mobile charges of bulk or interfacial regions of the material: semiconductor, insulators (dielectrics), ionic, and mixed electronic ionic [37]. Figure 3d shows the variation of impedance with frequency demonstrating the similarity with R and X curves. The close-up views of impedance analysis curves are shown as inset in figure. The impedance, Z is calculated by

$$Z = \sqrt{R^2 + X^2}. \quad (2)$$

In low frequency range (< 1 kHz), the Z decreases rapidly with the increasing Co concentration which indicates the decreased resistivity and enhanced conductivity of the samples [38]. Such activity naturally owes to the presence of space charge polarization [35, 36]. The crystallite size was reported to decrease with increasing Co concentration and leads to decrease Z due to the obstacle posed by grain boundaries. The decreased crystallite size of doped BFO helps to decease the bandgap energy [6] which enhances to decreases Z of the sample. Moreover, Z is reduced with oxygen (O_2) vacancies in doped sample. Dopant Co resulted in decreasing bond length (Fe–O), increasing bond angle (Fe–O–Fe) [6] and orbital overlaps are responsible to decrease Z of doped samples. The values of R, X, and Z

Table 1 Comparison of interplanar spacing and lattice constant between XRD and SAED methods

Sample	Method	Interplanar spacing of the crystallographic planes (Å)							Lattice constant (Å)	
		(012)	(104)	(202)	(024)	(112)	(214)	(220)	a	c
BFO	XRD	3.974	2.824	2.287	1.989	1.781	1.614	1.396	5.57764	13.86421
	SAED	4.032	2.857	2.298	1.980	1.785	1.619	1.387	5.69028	14.02568
BFCO	XRD	3.973	2.822	2.286	1.988	1.780	1.613	1.395	5.57544	13.85312
	SAED	4.024	2.865	2.291	1.995	1.787	1.615	1.380	5.65238	14.13364

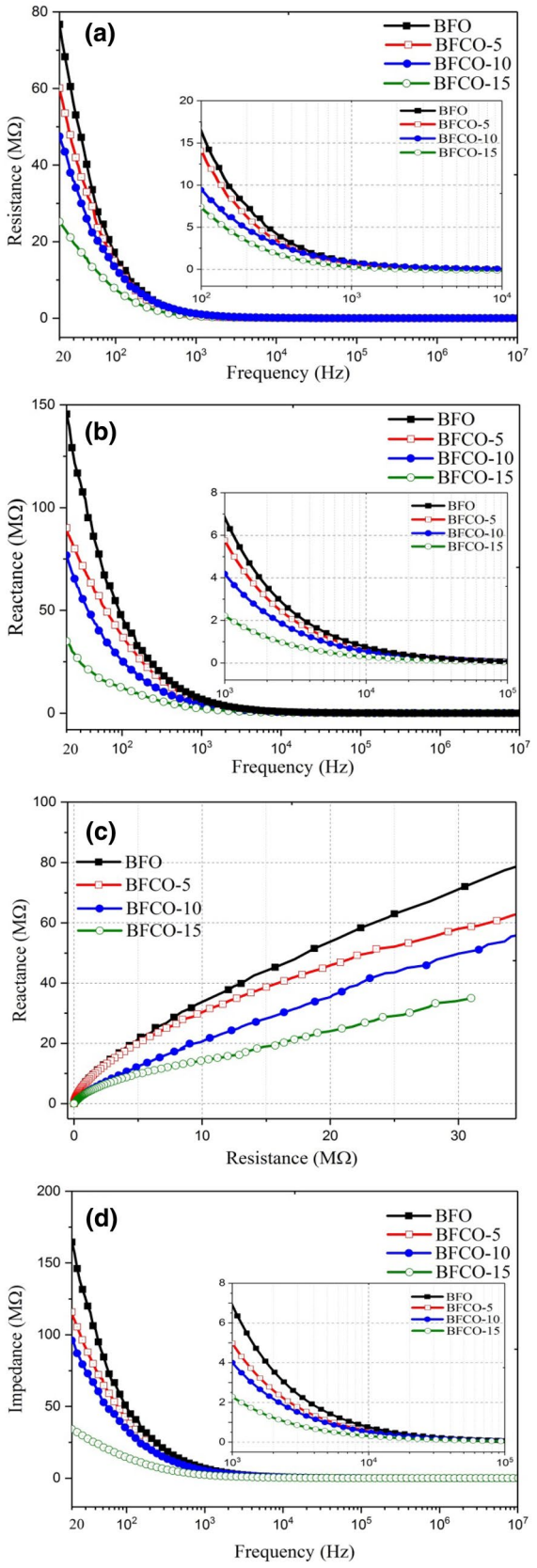

Fig. 3 **a** Resistance vs frequency, **b** reactance vs frequency, **c** reactance vs resistance and **d** impedance vs frequency curves of pure and doped BFO nanoparticles

for different samples at different frequencies are shown in Table 2.

Figure 4a shows the variation of AC resistivity (ρ_{AC}) with frequency at room temperature for pure and doped BFO samples. The electrical ρ_{AC} of pure and doped BFO nanoparticles was reduced significantly up to 10^4 Hz and remained almost constant above that. Co dopant has found to enhance the reduction of ρ_{AC}. This is because of leakage charges generated in piezoelectric grains of doped BFO across the low resistance path of the surrounding BFO grains [39].

Figure 4b represents AC conductivity (σ_{AC}) vs frequency in the range of 20 Hz–50 MHz at room temperature for pure and doped BFO samples. The plateau at $\leq 10^4$ Hz indicates frequency-independent or DC conductivity (σ_{DC}) which may be acquired by extra polluting conductivity values to the lower frequency [34]. At high frequency, the applied field promotes the jumping of charges between the localized regions resulting in enhanced σ_{AC} [40]. Therefore, in conduction process, hopping of 3d electrons along with Fe^{2+} and Fe^{3+} as well as Co^{2+} and Co^{3+} might play a vital role to enhance σ_{AC} [41]. The values of ρ_{AC} and σ_{AC} for different compositions at different frequencies are shown in Table 2.

There are two major factors that influence the σ_{AC} of BFO in high frequency (10^6) regime: (i) charge transportation and (ii) charge relaxation. The electrons migrate in the conductive materials when there are defects and interfaces in between adjacent layers [31]. The σ_{AC} of charge transport is satisfied by the following equation [42].

$$\frac{1}{\sigma_{AC}} = \rho_{AC} + \rho_{AC} = \frac{1}{\sigma_{AC_{mig}}}(\omega) + \frac{1}{\sigma_{AC_{hop}}}(\omega). \tag{3}$$

where $\sigma_{AC_{mig}}$ is the AC conductivity of electron migration and $\sigma_{AC_{hop}}$ is the AC conductivity of electron hopping. The Co doping in BFO has increased conductivity and decreased resistivity which may enhance the bulk photovoltaic effect in BFO thin films [4]. The dielectric properties of pure and doped BFO showed the frequency response in microwave application due to its structural distortion and defect. Also, the amount of doping influences dielectric properties in BFO nanoparticles [43].

3.4 Ferroelectric properties

The polarization vs electric field, P–E hysteresis loops measured at 100 Hz has been analyzed to study the effect of ferroelectric properties of pure and Co-doped BFO nanoparticles. The electric field-induced polarization was performed at room temperature with an applied electric field of 5–15 kV/cm. Figure 5a shows the P–E hysteresis loops of pure BFO nanoparticles, the magnifying view of which clearly displays the coercive field and remnant polarization (inset in Fig. 5a). The ferroelectricity generates in pure BFO

Table 2 Parameters of dielectric properties at different frequencies for pure and doped BFO nanoparticles

Parameter	Frequency (Hz)	BFO	BFCO-5	BFCO-10	BFCO-15
Resistance (MΩ)	20	77	60	47	31
	100	16	14	9.5	7.5
	1 k	0.87	0.57	0.3	0.2
Reactance (MΩ)	20	146	90	76	35
	100	45	35	25	14
	1 k	7	5.5	4.1	2.2
Impedance (MΩ)	20	164	115	96	35
	100	48	36	31	17
	1 k	7	4.8	3.9	2.3
AC resistivity (MΩ-m)	20	50	25	21	8.1
	100	21	13.6	10.3	3.7
	1 k	8	5.4	3.1	1.39
AC conductivity (S/m) × 10^{-3}	1 M	0.005	0.024	0.038	0.042
	10 M	0.064	0.105	0.151	0.184

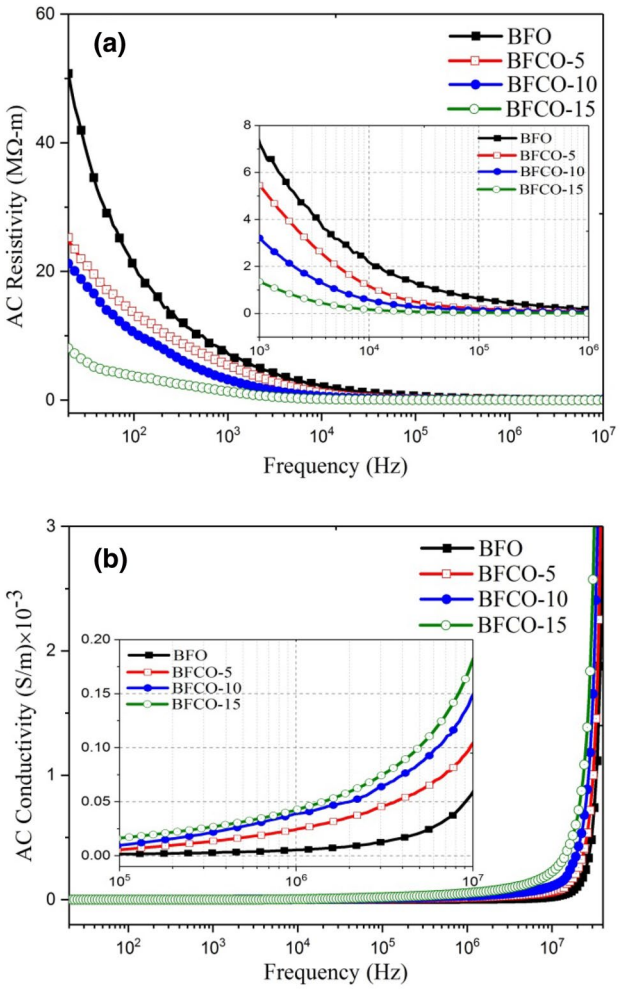

Fig. 4 **a** AC resistivity vs frequency and **b** AC conductivity vs frequency curves of pure and doped BFO nanoparticles

due to the presence of the Bi^{3+} ions of $6s^2$ lone pair electrons. The stereochemical action of the lone pair electrons was enhanced by the structural distortion due to Co doping into BFO lattice [44]. Ferroelectric properties are significantly enhanced in Co-doped BFO samples. Figures 5b–d shows the P–E hysteresis loops of doped BFO nanoparticles. The maximum polarization (P_{Max}) and remnant polarization (P_r) of doped BFO are much higher than pure one. This can occur as the charge reimbursement induced by the replacement of Co^{2+} for Fe^{3+} ions.

The enhanced ferroelectric property may also arise for changes in Fe–O bond length with Co-doped in BFO nanoparticles. The maximum polarization, remnant polarization, and coercive field of pure and doped BFO nanoparticles are summarized in Table 3. Inset in Fig. 5d represents the variation of P_r with Co concentrations. The values of P_r increase with increasing Co doping but the curve displaying a zigzag behavior; a similar trend was found in a previous study [12]. The Co dopant has shown to decrease the structural stability of BFO phases and increase the impurity phases ($Bi_2Fe_4O_9$), as shown in Fig. 1. This impurity phases may occur due to unbalanced charge and generate defects in the samples. These defects increase the electrical conductivity of the samples [45] and showed the largest P_r value in BFCO-15; similar result was found elsewhere [39]. This material can be useful for photovoltaic application.

The leakage current density (J) vs Electric field (E) plots of BFO, BFCO-5, BFCO-10, and BFCO-15 pelletized samples are shown in Fig. 6. According to ohmic conduction mechanism, J is directly related to thermally generated free electrons that can be explained as $J = e\mu N_e E$, where e is charge of an electron, μ is carrier mobility of free electron, N_e is density of thermally stimulated electrons, and E is electric field [46]. The free electron–hole pair concentration N_e sharply increases with reducing optical bandgap energy and

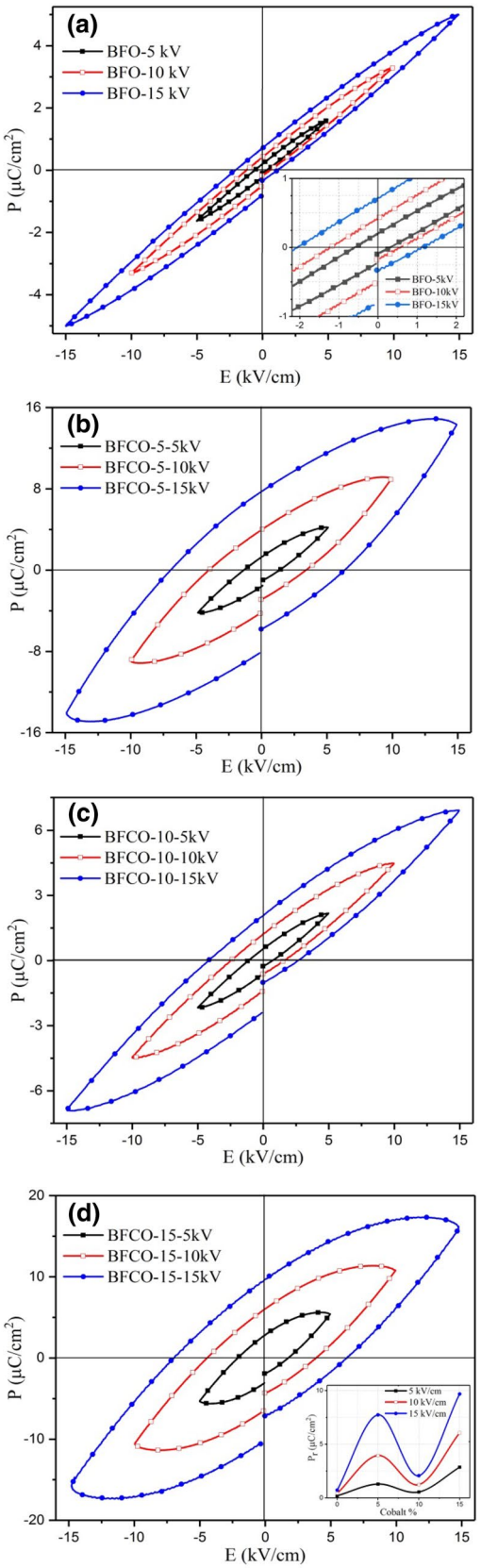

Fig. 5 P-E hysteresis loops of **a** BFO, **b** BFCO-5, **c** BFCO-10, and **d** BFCO-15 nanoparticles

thus raises the leakage current density [47]. The bandgap energy of BFO was decreased with increasing Co dopant concentration as shown in our previous research [6].

It is observed from Figs. 5 and 6 that the largest P_r value of doped BFO may be ascribed to the highest leakage current density of BFCO-15. Moreover, the zigzag behavior of P_r vs Cobalt % plot (inset in Fig. 5d) is due to the minimum leakage current density of 10% doped BFO when compared with 5% and 15% doped BFO nanoparticles.

3.5 Enhancement of magnetization

M–H hysteresis loop of the samples were captured at room temperature and plotted in Fig. 7. Magnetic parameters such as saturation magnetization (M_s), remnant magnetization (M_r), and coercive field (H_c) have been extracted and displayed in Table 4. It is clearly demonstrated that the magnetization value of pure BFO is very low which has significantly increased to large values of M_s and M_r with Co doping due mainly to the strong ferromagnetic nature of Co dopant. A substantial enhancement of M_s (0.67 to 7.07 emu/gm) and M_r (0.17 to 3.27 emu/gm) has been observed. A remarkable hysteresis effect and appearance of high coercive field along with the sharp magnetization increase are clearly observed. The expanded loops of pure and doped BFO are shown as inset in Fig. 7 for clear indication of M_r, M_s, and H_c deviation. It is also evident from the experimental results that the enhancement of the magnetization with increasing Co content is monotonic in contrast with the increase of coercive field, which is rather sluggish and/or slightly declining. But the nature of enhancement of M_r with increasing dopant concentration is in concomitant with magnetization value.

The M–H hysteresis loop of pure BFO nanoparticles is clearly demonstrated as weak ferromagnetic curve. This is because BFO is a G-type antiferromagnetic like a paramagnet due to local spin ordering of Fe^{3+} at room temperature [48]. There are many research works that indicate the influence of ferromagnetic as like as magnetic hysteresis for BFO due to secondary phases ($Bi_2Fe_4O_9$) [49]. Thus, the enhanced magnetization of Co-doped samples may be partly contributed from $Bi_2Fe_4O_9$ [50]. Furthermore, the contribution of secondary phase in magnetic ordering of BFO is insignificant due to its paramagnetic nature at room temperature [51].

It is evident from XRD patterns that the secondary phases of BFO increased with doping concentration of cobalt as shown in Fig. 1. The variation of magnetic moment and difference in ionic radii of Co^{2+} (0.745 Å) and Fe^{3+} (0.645 Å) interrupted the spiral spin structure of BFO. As a result, the enhancement of magnetization increases for Co^{2+} doping in pure BFO nanoparticles [47, 52, 53]. For nanoparticles, the surface-to-volume ratio is very high. The particle size is decreased with increasing Co doping concentration [6],

Table 3 Maximum polarization, remnant polarization, and coercive field of pure and doped BFO nanoparticles

Sample	Field applied (E) (kV/cm)	Maximum polarization (P_{Max}) (μC/cm^2)	Remnant polarization (P_r) (μC/cm^2)		Coercive field (E_c) (V/cm)	
			$-P_r$	P_r	$-E_c$	E_c
BFO	5	1.627	0.235	0.196	601	291
	10	3.322	0.522	0.426	1195	576
	15	4.996	0.836	0.725	2057	1107
BFCO-5	5	4.197	1.528	1.288	1357	1373
	10	9.019	4.263	3.956	4005	3406
	15	14.338	8.158	7.737	6945	6343
BFCO-10	5	2.177	0.618	0.547	1116	713
	10	4.481	1.425	1.233	2456	1597
	15	6.911	2.407	2.071	4177	2656
BFCO-15	5	5.397	3.082	2.857	2100	1753
	10	10.752	6.529	6.056	4435	3877
	15	16.052	10.578	9.686	6954	6230

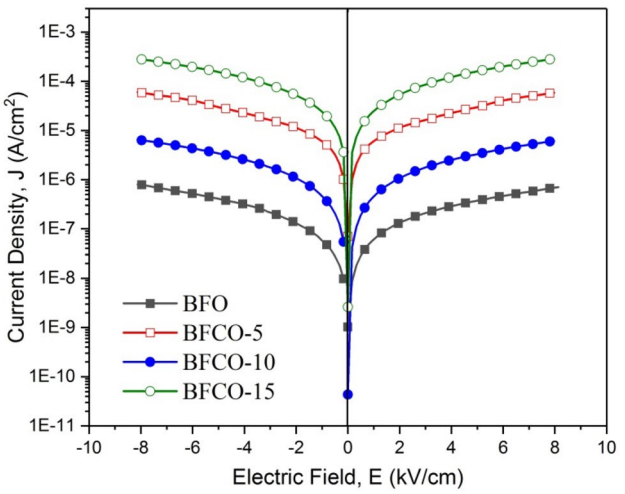

Fig. 6 Leakage current density vs Electric field plots of pure and Co-doped BFO nanoparticles

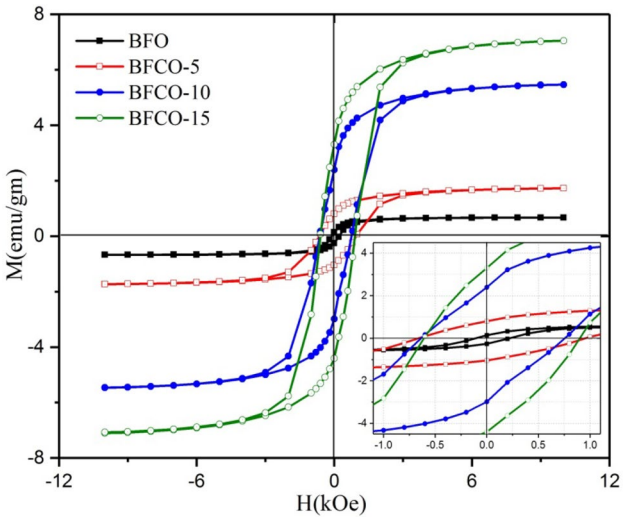

Fig.7 Magnetization vs magnetic field hysteresis loops for pure and doped BFO at room temperature

which formed the perfection and substantial involvement of the particles to enhance overall magnetization of doped samples by unpaired surface spins [54]. Next, the structural deformation for Co dopant may also contribute to the enhancement of magnetization [55]. Another two possible reasons may explain to improve the magnetic properties for Co^{2+} doped in pure BFO: (i) the replacement of Fe^{3+} ($3d^5$) with magnetically more active Co^{2+} ($3d^6$) can enhance magnetic properties in the samples and (ii) a strong magnetic coupling between Co^{2+} and Fe^{3+} under 180 degree super exchange relations may be the other reason to enhance magnetization in Co-doped BFO nanoparticles [56].

Simultaneously, H_c also increased with Co^{2+} doped in BFO samples. The main reason to increase H_c for magnetic materials are magnetocrystalline anisotropy and magnetoelastic anisotropy [57]. The squareness ratio (SQR) M_r/M_s indicates how square is the hysteresis loop for memory devices: it should be as large as possible. The small value of SQR specifies the isotropic nature of the sample [58]. In accordance with Stoner Wohlfarth model, the value of M_r/M_s is 0.5 for single domain particles along the easy axis and randomly oriented [59]. The enhanced SQR of doped BFO indicates its preference for memory devices. A significant enhancement of H_c in Co-doped BFO from 216 to 903 Oe has been observed. If the value of H_c is greater than 100 Oe, the materials are considered as hard magnetic. The high value of H_c indicates the hardness to demagnetize the materials. Hard magnetic materials are normally used in magnetic recording devices. Moreover, recently it has been found that BFO has good electromagnetic interference (EMI) shielding performance and absorption-domination mechanism [60].

Table 4 Saturation magnetization, remnant magnetization, coercive field, and SQR of pure and doped BFO nanoparticles

Sample	Saturation magnetization (M_s) (emu/gm)	Remnant magnetization (M_r) (emu/gm)		Coercive field (H_c) (kOe)		SQR
		$-M_r$	M_r	$-H_c$	H_c	
BFO	0.67	0.280	0.170	0.115	0.216	0.34
BFCO-5	1.73	1.02	0.771	0.635	0.966	0.52
BFCO-10	5.46	3.00	2.43	0.641	0.750	0.50
BFCO-15	7.07	4.38	3.27	0.608	0.903	0.54

4 Conclusion

Well crystalline pure and Co-doped BFO nanoparticles have successfully been synthesized by sol–gel method. The structural, electrical conductivity, and multiferroic properties have been studied in detail. The crystallite size of cobalt-doped BFO was found to be decreased to 45 nm. Rietveld refinement of XRD has confirmed that Co atoms were effectively incorporated into the parent lattice. TEM images confirmed irregular shape morphology, while the particle size of doped sample was found to be smaller than that of pure sample. SAED patterns exhibited polycrystalline nature of samples and conformity of crystal parameters obtained from XRD measurements. Dielectric analysis showed that the significant reduction in resistive properties and enhanced electrical conductivity with increasing Co dopant concentration. The ferroelectric hysteresis loop of pure BFO has found to be affected rapidly by the replacement of Co for Fe. The Co-doped in BFO increased the P_r and H_c which is related to increase conductivity. Co-doped BFO guided the structural transformation from R3c to $Pn2_1a$ symmetry that was shown to have a substantial effect on enhancement of magnetization. An outstanding improvement in ferromagnetic property, $M_s = 7.07$ emu/g has been observed for BCFO-15 nanoparticles. The SQR ratio of doped BFO is found to be about 0.5 which indicates that the materials may be ideal for memory devices. Thus, it exposes a step ahead for the scope of magnetization compared to applied electric fields and vice versa for memory device applications.

Acknowledgements We acknowledge the experimental support obtained from the Department of Glass and Ceramic Engineering, Bangladesh University of Engineering and Technology (BUET), Dhaka. Special thanks to Dr. Nazrul Islam (Principal Scientific Officer) and Dr. Harinarayan Das (Senior Scientific Officer), Materials Science Division, Atomic Energy Centre, Dhaka to assist the VSM and TEM measurement.

References

1. W. Eerenstein, N.D. Mathur, J.F. Scott, Nature **442**, 759 (2006)
2. S.W. Cheong, M. Mostovoy, Nature Mater. **6**, 13 (2007)
3. R. Ramesh, N.A. Spaldin, Nature Mater. **6**, 21 (2007)
4. W. Ji, K. Yao, Y.C. Liang, Adv. Mater. **22**, 1763 (2010)
5. M.M. Rhaman, M.A. Matin, M.N. Hossain, F.A. Mozahid, M.A. Hakim, M.F. Islam, J. Electron. Mater. **47**, 6954 (2018)
6. M.M. Rhaman, M.A. Matin, M.N. Hossain, F.A. Mozahid, M.A. Hakim, M.F. Islam, Bull. Mater. Sci. **42**, 190 (2019)
7. Y. Li, W.-Q. Cao, J. Yuan, D.-W. Wang, M.-S. Cao, J. Mater. Chem. C **3**, 9276 (2015)
8. N.A. Hill, J. Phys. Chem. B **104**, 6694 (2000)
9. J. Wang, J.B. Neaton, H. Zheng, V. Nagarajan, S.B. Ogale, B. Liu, D. Viehland, V. Vaithyanathan, D.G. Schlom, U.V. Waghmare, N.A. Spaldin, K.M. Rabe, M. Wuttig, R. Ramesh, Science **299**, 1719 (2003)
10. Ch Yang, J.S. Jiang, F.Z. Qian, D.M. Jiang, ChM Wang, W.G. Zhang, J. Alloys Compd. **507**, 29 (2010)
11. F. Desouki, New J. Glass Ceram. **5**, 59 (2015)
12. F. Chang, N. Zhang, F. Yang, S. Wang, G. Song, J. Phys. D Appl. Phys. **40**, 7799 (2007)
13. U. Fazal, M.S. Awan, Z. Wazir, S. Irfan, A. ulHaq, Pak J. Chem. Society **40**, 886 (2018)
14. Y.A. Chaudhari, C.M. Mahajan, P.P. Jagtap, S.T. Bendre, J. Adv. Ceram. **2**, 135 (2013)
15. I. Sosnowska, W. Schäfer, W. Kockelmann, K.H. Andersen, I.O. Troyanchuk, Appl. Phys. A **74**, S1040 (2002)
16. D.P. Dutta, B.P. Mandal, R. Naik, G. Lawes, A.K. Tyagi, J. Phys. Chem. C **117**, 2382 (2013)
17. M. Polomska, W. Kaczmarek, Z. Pajak, J. Phys. Status Solidi A **23**, 567 (1974)
18. I. Sosnowska, T.P. Neumaier, E. Steichele, J. Phys. C Solid State Phys. **15**, 4835 (1982)
19. P. Banerjee, A. Franco Jr., J Mater Sci Mater Electron **27**, 6053 (2016)
20. P. Kharel, S. Talebi, B. Ramachandran, A. Dixit, V.M. Naik, M.B. Sahana, C. Sudakar, R. Naik, M.S.R. Rao, G. Lawes, J. Phys. Condens. Matt. **21**, 036001 (2009)
21. J. Ray, A.K. Biswal, S. Acharya, V. Ganesan, D.K. Pradhan, P.N. Vishwakarma, J. Magn. Magn. Mater. **324**, 4084 (2012)
22. J. Allibe, S. Fusil, K. Bouzehouane, C. Daumont, D. Sando, E.J.C. Deranlot, M. Bibe, A. Barthelemy, Nano Lett. **12**, 1141 (2012)
23. M.-S. Cao, X.-X. Wang, M. Zhang, J.-C. Shu, W.-Q. Cao, H.-J. Yang, X.-Y. Fang, J. Yuan, Adv. Funct. Mater. **29**, 1807398 (2019)
24. M. A. Matin, M. N. Hossain, M. H. Rizvi, M. A. Zubair, M. A. Hakim, A. Hussain, M.F. Islam, *EPTC Conference Proceeding* (2017), pp. 1–6.
25. G. Catalan, J.F. Scott, Adv. Mater. **21**, 2463 (2009)
26. I. Sosnowskat, T. Peterlin-Neumaier, E. Steichele, J. Phys. C Solid State Phys. **15**, 4835 (1982)
27. X. Bai, J. Wei, B. Tian, Y. Liu, T. Reiss, N. Guiblin, P. Gemeiner, B. Dkhil, I.C. Infante, J. Phys. Chem. C **120**, 3595 (2016)
28. M.A. Matin, M.M. Rhaman, M.N. Hossain, F.A. Mozahid, M.A. Hakim, M.H. Rizvi, M.F. Islam, Trans. Electr. Electron. Mater. **20**, 485 (2019)
29. C.T. Munoz, J.P. Rivera, A. Monnier, H. Schmid, Japan. J. Appl. Phys. Suppl. **24**, 1051 (1985)

30. J.R. Teague, R. Gerson, W.J. James, Solid State Commun. **8**, 1073 (1970)
31. M. Zhang, X.-X. Wang, W.-Q. Cao, J. Yuan, M.-S. Cao, Adv. Opt. Mater. **7**, 1900689 (2019)
32. B. Behera, P. Nayak, R.N.P. Choudhary, Cent. Eur. J. Phys. **6**, 289 (2008)
33. J. Płcharski, W. Weiczorek, Solid State Ionics **28**, 979 (1988)
34. M.A. Matin, M.N. Hossain, M.A. Ali, M.A. Hakim, M.F. Islam, Results Phys. **12**, 1653 (2019)
35. S.G. Doh, E.B. Kim, B.H. Lee, J.H. Oh, J. Magn. Magn. Mater. **272**, 2238 (2004)
36. M. Hashim, S.E. Shirsath, S. Kumar, R. Kumar, A.S. Roy, J. Shah, R.K. Kotnala, J. Alloys Compd. **549**, 348 (2013)
37. S.C. Mazumdar, M.N.I. Khan, M.F. Islam, A.K.M. Akther Hossain, J. Magnet. Magnet. Mater. **401**, 443 (2016)
38. M.D. Rahaman, S.H. Setu, S.K. Saha, A.K.M. Akther Hossain, J. Magnet. Magnet. Mater. **385**, 418 (2015)
39. M.M. Rhaman, M.A. Matin, M.A. Hakim, M.F. Islam, Mater. Res. Express **6**, 125080 (2019)
40. J. Kolte, P.H. Salame, A.S. Daryapurkar, P. Gopalanl, AIP Adv. **5**, 097164 (2015)
41. M.D. Rahaman, S.K. Saha, T.N. Ahmed, D.K. Saha, A.K.M. Akther Hossain, J. Magnet. Magnet. Mater. **371**, 112 (2014)
42. M.-S. Cao, W.-L. Song, Z.-L. Hou, Bo Wen, J. Yuan, Carbon **48**, 788 (2010)
43. Y. Li, X. Fang, M. Cao, Sci. Rep. **6**, 24837 (2016)
44. H.M. Christen, J.H. Nam, H.S. Kim, A.J. Hatt, N.A. Spaldin, Phys. Rev. B **83**, 144107 (2011)
45. Z.X. Cheng, A.H. Li, X.L. Wang, S.X. Dou, K. Ozawa, H. Kimura, S.J. Zhang, T.R. Shrout, J. Appl. Phys. **103**, 07E507 (2008)
46. C. Wang, M. Takahashi, H. Fujino, X. Zhao, E. Kume, T. Horiuchi, S. Sakai, J. Appl. Phys. **99**, 054104 (2006)
47. M. Gratzel, Photoelectrochemical cells. Nature **414**, 338e344 (2001)
48. H. Hayashi, A. Sato, T. Azumi, Y. Udagawa, Phys. Rev. B **73**, 134405 (2006)
49. Y.K. Jun, W.T. Moon, C.M. Chang, H.S. Kim, H.S. Ryu, J.W. Kim, K.H. Kim, S.H. Hong, Solid State Comm. **135**, 113 (2005)
50. H. Naganuma, J. Miura, S. Okamura, Appl. Phys. Lett. **93**, 052901 (2008)
51. Y.L. Han, W.F. Liu, P. Wu, X.L. Xu, M.C. Guo, G.H. Rao, S.Y. Wang, J. Alloys Compd. **661**, 115 (2016)
52. Y. Chen, Wu Qingsheng, J. Zhao, J. Alloys Compd. **487**, 599 (2009)
53. Z. Quan, W. Liu, H. Hu, S. Xu, B. Sebo, G. Fang, M. Li, X. Zhao, J. Appl. Phys. **104**, 084106 (2008)
54. F.Z. Huang, Z.J. Wang, X.M. Lu, J.T. Zhang, K.L. Min, W.W. Lin, R.X. Ti, T.T. Xu, J. He, C. Yue, J.S. Zhu, Sci. Rep. **3**, 2907 (2013)
55. M.M. Shirolkar, C.S. Hao, X.L. Dong, T. Guo, L. Zhang, M. Li, H.Q. Wang, Nanoscale **6**, 4735 (2014)
56. L. Penga, H. Dengb, J. Tiana, Q. Rena, C. Penga, Z. Huanga, P. Yanga, J. Chua, Appl. Surf. Sci. **268**, 146 (2013)
57. K. Chakrabarti, K. Das, B. Sarkar, S. Ghosh, S.K. De, G. Sinha, J. Lahtinen, Appl. Phy. Lett. **101**, 042401 (2012)
58. S.E. Shirsath, B.G. Toksha, K.M. Jadhav, Mater. Chem. Phys. **117**, 163 (2009)
59. E.C. Stoner, E.P. Wohlfarth, Philos. Trans. R. Soc. A **240**, 599 (1948)
60. Y. Li, N.N. Sun, J. Liu, X.H. Hao, J.H. Du, H.J. Yang, X.W. Li, M.S. Cao, Compos. Sci. Technol. **159**, 240 (2018)